

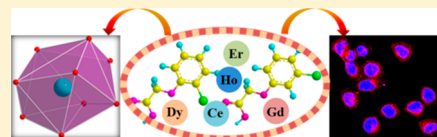
Click Chemistry-Assisted Synthesis of a β -D-Galactose-Targeted SiO₂@RC Shell–Core Structure as a Nanoplatfor for Metal-Based Complex Delivery

Xiuling Xu, Fan Hu, and Qi Shuai*[✉]

Shaanxi Key Laboratory of Natural Products & Chemical Biology, College of Chemistry & Pharmacy, Northwest A&F University, Yangling, Shaanxi 712100, People's Republic of China

Supporting Information

ABSTRACT: A facile reversed-phase microemulsion method was used to synthesize shell–core nanospheres of SiO₂@RCs (SiO₂-encapsulated rare-earth metal complexes). β -D-Galactose was then grafted onto the surfaces of the nanospheres through the copper(I)-catalyzed azide–alkyne cycloaddition click reaction for targeted delivery. The chemical characteristics and surface profiles of the nanocarriers were investigated by Fourier transform infrared spectroscopy, dynamic light scattering, transmission electron microscopy, and scanning electron microscopy. A high-efficiency microwave synthesis method was applied to prepare five complex cores by the reaction of different rare-earth metal salts with two isomeric ligands, *o*-CPA (2-chlorophenoxyacetic acid) and *m*-CPA (3-chlorophenoxyacetic acid). The crystal structures of the five synthesized RC cores were confirmed through X-ray diffraction, which revealed the formulas of five RCs, [Dy(*o*-CPA)₃(H₂O)]·H₂O RC₁, [Ho(*o*-CPA)₃(H₂O)]·H₂O RC₂, 2[Er(*m*-CPA)₃(H₂O)]·3H₂O RC₃, 2[Gd(*m*-CPA)₃(H₂O)]·3H₂O RC₄, and [Ce₂(*m*-CPA)₆(H₂O)₃]·2H₂O RC₅. An *in vitro* cell study revealed that all RCs exhibited certain anticancer activities. RC₂, in particular, showed the strongest cytotoxicity against HepG2 cells. The enhanced cell permeability and drug retention considerably improved the cytotoxicity of all SiO₂@RC₂-gal relative to that of RC₂. The selective uptake of the β -D-galactose-conjugated nanospheres by HepG2 cells through mechanisms mediated by cell surface receptors resulted in fewer side effects on extrahepatic tissues. Our contribution provides a novel design concept of a target SiO₂@RCs-gal nanocarrier for delivering affordable antitumor complexes in cancer therapy.



INTRODUCTION

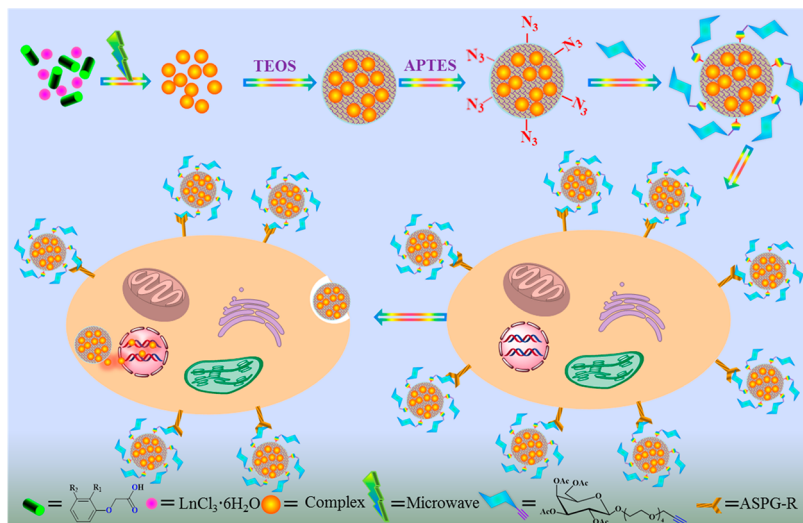
Rosenburg's significant discovery that cisplatin shows a favorable curative effect on a variety of cancers has inspired an increasing number of chemists to develop metal-based complexes with antitumor activities.^{1–4} Rare-earth metal complexes (RCs) typically have a higher affinity for tumor tissues than for normal tissues.^{5–7} Recent studies have revealed that acylhydrazone, amino acid, polypyridyl, and quercetin show enhanced inhibitory effects on several kinds of cancer cells after coordination with rare-earth metals.^{8–14} In addition, the lower cost of RCs relative to that of platinum-based anticancer complexes has driven researchers to develop RC-based antitumor agents.¹⁵ Nevertheless, despite their antitumor activities, damage to normal cells is difficult to avoid as a side effect given the weak specific recognition of RCs.^{16–19} Therefore, the development of target nanocarriers with good specificity and favorable biological compatibility is particularly urgent for the delivery of affordable metal-based complexes in cancer therapy.

Carbohydrates mainly mediate recognition events during tumor development and progression by interacting with glycoproteins.^{20–23} The expression of glycoproteins on the cell surface may drastically change after carcinogenesis. For example, the cell surfaces of human liver tumor cell line HepG2 overexpress the asialoglycoprotein receptor (ASGP-R), which specifically binds to β -D-galactose and lactose.^{24,25}

However, the binding force between carbohydrates and glycoprotein is very weak. In 1995, Y. C. Lee first proposed the concept of the “glycoside cluster effect”, which can be explained as follows: carbohydrate molecules tend to aggregate during carbohydrate–glycoprotein interactions. This behavior causes the strength of the interaction between carbohydrates and glycoproteins to increase exponentially.²⁶ Therefore, the application of glyconanoparticles enables the highly multivalent method of interaction with ASGP-R for targeted liver cancer therapy and high concentrations of drugs to localize in a small area. These phenomena collectively weaken the side effects of the loaded antitumor drugs on extrahepatic tissues.^{27,28}

Mesoporous silica nanocarriers have attracted considerable attention in the area of drug delivery for their distinctive advantages of a larger surface area and a larger micropore volume, variable pore sizes, excellent surface properties, high mechanical and chemical stability, and excellent biocompatibility.^{29–31} Via the enhancement of cell permeability and drug retention (EPR) effect, the concentration of the drug near the tumor will increase passively through the transport of nanoparticles.^{32,33} In addition, the surfaces of the silica sphere were grafted with plenty of silanol groups that were chemically

Received: May 16, 2018

Scheme 1. Illustration of the SiO₂@RCs-gal Design Strategy and Receptor-Mediated Endocytosis

active and easily reacted with other functional groups. Therefore, it is advantageous to further graft other functional molecules, such as targeting molecules.³⁴ Considerable effort has been made to modify mesoporous silica nanocarriers with different functional groups, such as amine, epoxide, or thiol.^{35–37} The copper(I)-catalyzed azide–alkyne cycloaddition (CuAAC) click reaction is an amazing and prospective synthesis approach for its distinct “click” properties of high yield, high product quality, low cost, and no large amounts of byproducts.^{38–42} To date, functionalization with azide groups through click chemistry has emerged as a momentous contribution to surface modification of mesoporous silica. Using the click chemistry reaction, Park et al. used the cyclodextrin plug connected to cover the pores of mesoporous silica nanocarriers in 2010.⁴³ Given the advantages mentioned above, click chemistry methods have become more attractive tools for the site-specific immobilization between targeting molecules and mesoporous silica nanoparticles.

In this study, by rapid microwave methods, RCs were successfully synthesized with a shorter reaction time. It is vital to effectively control the release of RCs and restrain the rapid dissolution of the nanospheres; thus, a film of silica prepared by TEOS was used to coat the RCs. Employing the condensation reaction of APTES, azide groups were joined to the surface of silica nanocarriers. Alkyne β -D-galactose was selected to achieve target delivery because of its high affinity for ASPG-R (ASPG-R was overexpressed on the surface of HepG2 cells). Moreover, alkynylated galactose was easily grafted onto the surface of mesoporous silica nanocarriers by the CuAAC click reaction. Via the conjugation of β -D-galactose, the spheres were selectively ingested by HepG2 cells through mechanisms that are implemented by cell surface receptors (Scheme 1).

EXPERIMENTAL SECTION

Materials and Reagents. All of the chemicals were used as received. HoCl₃·6H₂O, DyCl₃·6H₂O, ErCl₃·6H₂O, GdCl₃·6H₂O, CeCl₃·6H₂O, Triton X-100, 2-chlorophenol, hexyl alcohol, 3-chlorophenol, ethyl chloroacetate, K₂CO₃, KI, NaH, bis[2-(2-hydroxyethoxy)ethyl] ether, 3-bromopropyne, β -D-galactose, iodine, acetic anhydride, ammonium hydroxide, sodium thiosulfate, BF₃·OEt₂, 3-chloropropyltrithoxysilane, sodium azide, tetrabutylammonium iodide, tetraethyl orthosilicate, sodium ascorbate, CuSO₄·5H₂O,

and cyclohexane were of analytical grade and obtained from Acros Organics.

Apparatus. ¹H nuclear magnetic resonance (NMR) and ¹³C NMR spectra were recorded with a Bruker AVANCEIII 500 MHz spectrometer. Microwave-assisted synthesis was performed on a CEM Discover SP single-mode cavity instrument. Elemental analyses were performed with a Vario MACRO cube elemental analyzer. Fourier transform infrared spectroscopy (FT-IR) data were recorded using the BRUKER TENSOR 27 spectrophotometer. Transmission electron microscopy (TEM) images were taken with an FEI TECNAI G2 SPIRIT BIO instrument. Scanning electron microscopy (SEM) (FEI Nova Nano SEM 450) was used to scan morphology. Confocal laser scanning microscopy (CLSM) was performed with a REVOLUTION WD instrument. Viability was determined using a Perlong DNM-9062 microplate reader.

Preparation of RC₁–RC₅. While the mixture was being continuously stirred, a NaOH solution (0.2 mmol) was slowly added to an ethanol solution of *o*-HCPA or *m*-HCPA (Scheme S1 and Figures S1–S4) to adjust the pH to 7. One-third equivalent of LnCl₃·6H₂O (Ln = Dy, Ho, Er, Gd, or Ce) was dissolved in deionized water and added to the mixture mentioned above while it was being stirred. Then the mixture was placed into a microwave tube (25 mL) and heated by a CEM Discover SP single-mode cavity instrument (100 °C, 100–200 W) under autogenous pressure for 1 h. The mixture was cooled and filtered. For colorless crystals of RC₁–RC₅, one part can be collected directly from the filter paper and others can be acquired by further evaporating the filtrate for several days. RC₁–RC₅ have high stabilities and can maintain a complete structure for a long time at room temperature. For RC₁, C₂₄H₂₂Cl₃DyO₁₁: C, 38.13; H, 2.91. Found: C, 38.12; H, 2.92. IR data: 3494 b, 1560 s, 1474 s, 1429 s, 1132 s, 1080 s, 596 m cm⁻¹. For RC₂, C₂₄H₂₂Cl₃HoO₁₁: C, 38.01; H, 2.90. Found: C, 38.02; H, 2.92. IR data: 3495 b, 1569 s, 1560 s, 1478 s, 1136 s, 1082 s, 595 m cm⁻¹. For RC₃, C₄₈H₄₆Cl₆Er₂O₂₃: C, 37.50; H, 2.99. Found: C, 37.60; H, 2.98. IR data: 3452 b, 1607 s, 1475 s, 1432 s, 1222 s, 1071 s, 598 m cm⁻¹. For RC₄, C₄₈H₄₆Cl₆Gd₂O₂₃: C, 37.94; H, 3.03. Found: C, 37.95; H, 3.04. IR data: 3456 b, 1603 s, 1481 s, 1426 s, 1220 s, 1069 s, 611 m cm⁻¹. For RC₅, C₄₈H₄₆Ce₂Cl₆O₂₃: C, 38.82; H, 3.10. Found: C, 38.81; H, 3.09. IR data: 3409 b, 1870 s, 1488 s, 1429 s, 1173 s, 1067 s, 611 m cm⁻¹ (see Figures S5–S9).

Preparation of SiO₂@RC-N₃ Nanoparticles. In a round-bottom flask (50 mL), 2 μ mol of RC was dissolved in 0.50 mL of deionized water. A mixture of 5.78 mmol of Triton X-100, 69.42 mmol of cyclohexane, and 14.45 mmol of hexyl alcohol was quickly added under ultrasonic conditions for 0.5 h. Then the mixture mentioned above was placed on the shaking bath (100 rpm) at room temperature for 24 h; 0.10 mL of tetraethyl orthosilicate and 0.10 mL of APTES

(see Scheme S2 and Figures S10 and S11 for details) were then separately added under ultrasonic conditions for an additional 0.5 h, followed by 0.06 mL of ammonium hydroxide being added in a dropwise manner. Then the mixture was placed on the shaking bath (100 rpm) for 24 h. Ten milliliters of acetone can be used to demulsify. The solid was washed at least three times with water (50 mL) and ethanol (50 mL) after centrifugation (10000 rpm, 15 min), and then the solid placed in a vacuum oven at 25 °C for 16 h.

Conjugation of Alkyne β -D-Galactose to SiO₂@RC-N₃ Nanoparticles by the CuAAC Click Reaction. To a H₂O/CH₂Cl₂ suspension (1:1, 40 mL) of SiO₂@RC-N₃ (50 mg) was carefully added 0.55 mg of 2-[2-(2-propargyloxyethoxy)ethoxy]ethanol-2,3,4,6-tetra-*O*-acetyl- β -D-galactopyranoside (see Schemes S3–S5 and Figures S12–S16 for details), followed by the addition of a sodium ascorbate (2.75 mg, 0.014 mmol) solution and 7.0 mg of copper(II) sulfate pentahydrate (0.028 mmol) that was dissolved in 3 mL of deionized water. The reaction mixture mentioned above was stirred at room temperature for 24 h. The nanoparticles were gathered by centrifugation (10000 rpm, 10 min) of the suspension and washed sequentially with 50 mL of deionized water and acetone. Then the final products were placed in a vacuum oven at 25 °C for 16 h.

X-ray Crystal Structure Determination. All the single-crystal data were collected on a Bruker SMART CCD diffractometer equipped with a graphite monochromatized Mo K α microfocus X-ray source ($\lambda = 0.71073$ Å) in ω scan mode at 298(2) K. Data reduction was performed with the Bruker SAINT package. All non-hydrogen atoms were refined anisotropically.⁴⁴ Further details of the X-ray structural analyses are given in Table S1, and selected angles and bond lengths for RC₁–RC₅ are listed in Table S2. The CCDC numbers were 1561412 for RC₁, 1561424 for RC₂, 1561426 for RC₃, 1561432 for RC₄, and 1561433 for RC₅. All the crystal data can be obtained from The Cambridge Crystallographic Data Centre via www.ccdc.cam.ac.uk/data_request/cif.

Cytotoxicity and Proliferation Activity Determined by the MTT Assay. For RCs, SiO₂-gal, and SiO₂@RC-gal nanocarriers, the cytotoxicity and antiproliferative activity have been systemically evaluated on cancer cell (HepG2) and normal cell (293T) lines. Cell viability and proliferation were investigated by the MTT assay. HepG2 and 293T cells were seeded in 96-well plates (7×10^3 cells/well) at 37 °C with 5% CO₂ for 24 h. The free RC₂, SiO₂-gal, and RC₂@SiO₂-gal nanoparticles were treated with two kinds of cells for 24 h. Then, cells were washed with phosphate-buffered saline (PBS) at least three times. Then MTT solutions (10 μ L, 5 mg/mL) and 90 μ L of 1640 culture medium were added to every well. After this operation had been completed, the cells were incubated for 4 h. After the medium had been removed, the crystals were dissolved in dimethyl sulfoxide. OD (optical density) data were collected with the microplate reader. The data represent mean values \pm the standard deviation.

$$\text{cell viability (\%)} = \frac{\text{OD of test group} - \text{OD of blank group}}{\text{OD of control group} - \text{OD of blank group}} \times 100$$

RESULTS AND DISCUSSION

Features of the Novel Crystal Structure. *Description of the Crystal Structure of [Dy(*o*-CPA)₃(H₂O)] \cdot H₂O RC₁.* RC₁ and RC₂ are isostructural, so we describe only RC₁ in detail for the sake of clarity. Single-crystal X-ray diffraction (XRD) analysis shows that RC₁ crystallizes in a monoclinic crystal system and belongs to space group C2/c. As displayed in Figure 1, one crystallographically unique Dy(III) ion, one coordinated water, three *o*-CPA ligands, and one lattice water molecule were found in every asymmetric structure. The Dy(III) atom is nine-coordinated (Figure 2a), which was completed by eight carboxyl oxygen atoms (O1, O7, O8B, O4B, O5, O2B, O1A, and O4) and O1W from coordinated water molecules.

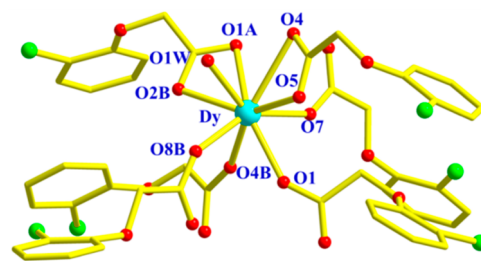


Figure 1. Local coordination environment around Dy(III).

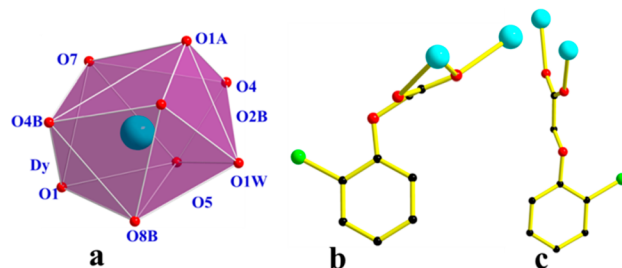


Figure 2. (a) Coordination geometry and (b and c) carboxyl coordination modes of RC₁.

In Figure 2a, the Dy(III) cation is located in a mildly distorted tricapped triangular prism completed by three planes (O1A–O1W–O8B–O4B, O1A–O1W–O5–O7, and O4B–O8B–O5–O7), in which three O atoms (O2B, O4, and O1) are located at the cap positions. The length of the Dy–O covalent bond is 2.295(3)–2.838(4) Å.⁴⁵

In RC₁, the carboxyl group from the *o*-CPA ligand is completely deprotonated, which displays a coordination mode of $\mu_2\text{-}\eta^1\text{:}\eta^2$ and $\mu_2\text{-}\eta^1\text{:}\eta^1$ (Figure 2b,c). Neighboring Dy(III) ions are linked through the two coordination modes, generating countless metal-based one-dimensional (1D) chains with a zigzag arrangement appearing alternatively along the *c* axis (Figure S17). The Dy–Dy–Dy angle (α) of the adjacent atoms is 149.487(9)°, and the distances (d_1) of the neighboring Dy(III) ions are 4.1772(15) Å. Further analysis of the crystal packing from Figure S17 reveals that the adjacent 1D chain can be self-assembled into a two-dimensional (2D) layer (Figure S18), and the 2D layer can be further assembled into a three-dimensional network by hydrogen bonds (Figures S19).

*Description of the Crystal Structure of [Er(*m*-CPA)₃(H₂O)]₂ \cdot 3H₂O RC₃.* RC₃ and RC₄ are isostructural, so we describe only RC₃ in detail for the sake of clarity. In Figure 3, single-crystal XRD analysis of [Er(*m*-CPA)₃(H₂O)]₂ \cdot 3H₂O revealed a dinuclear Er(III) complex exists. RC₃ crystallizes in a monoclinic crystal system and belongs to the space group C2/c. The coordination environment of Er(III) is shown in Figure 3. The structure of RC₃ is composed of two unique Er(III) atoms, six *m*-CPA molecules, two coordinated water molecules, and three lattice water molecules. As illustrated in Figure 4a, similar to the case in RC₁ and RC₂, the nine-coordinate Er(III) ion is located in a mildly distorted tricapped triangular prism completed by three planes (O8–O5A–O7A–O4, O8–O5A–O1WA–O1, and O7A–O4–O1–O1WA), in which three O atoms (O4, O2B, and O1) are located at the cap positions. The eight oxygens (O1, O1A, O2, O4, O4A, O5A, O7A, and O8) come from the carboxylate, and one oxygen (O1WA) derives from coordinated water molecules. Er–O bond lengths extend from 2.311(2) to 2.677(2) Å.⁴⁶

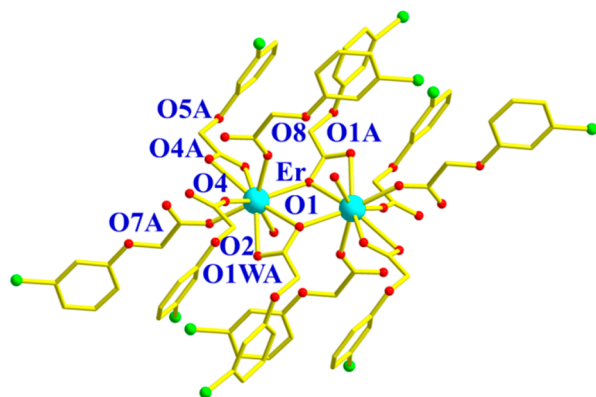


Figure 3. Local coordination environment around Er(III).

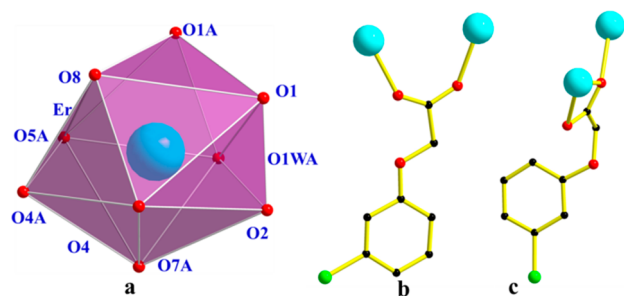


Figure 4. (a) Coordination geometry and (b and c) carboxyl coordination modes of RC_3 .

Two Er(III) ions are connected by carboxylate groups, which display a 1D chain in the a – b plane (Figure S20). The carboxyl group from the o -CPA ligand displays a coordination mode of μ_2 - η^1 : η^2 and μ_2 - η^1 : η^1 (Figure 4b,c). The neighboring chains extend into the 2D layer through hydrogen bonds (Figure S21).

Description of the Crystal Structure of $[Ce_2(m\text{-CPA})_6(H_2O)_3]\cdot 2H_2O$ RC_5 . The coordination environment around the Ce(III) centers in RC_5 can be seen from Figure 5. The Ce(III) ions lie in decacoordinate environments,

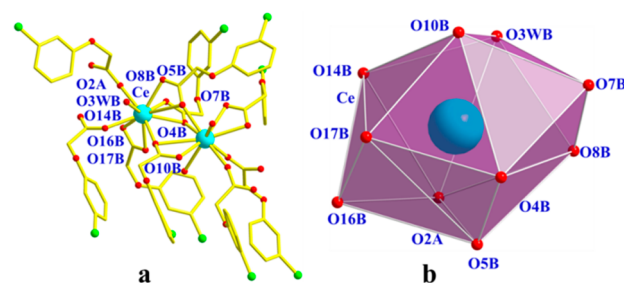


Figure 5. Local coordination environment and polyhedron around Ce(III) in RC_5 .

consisting of nine oxygen atoms (O2A, O4B, O5B, O7B, O8B, O10B, O14B, O16B, and O17B) that come from the carboxyl group of unique m -CPA ligands, and the only oxygen atom comes from coordination water. In the molecular units, the centric Ce(III) is in a severely distorted dicapped square antiprism environment. The lengths of Ce–O bonds range from 2.435(6) to 2.845(7) Å with an average value of 2.561 Å.⁴⁷

In RC_5 , the carboxyl groups of m -CPA ligands provide two types of coordination modes: μ_2 - η^1 : η^1 and μ_2 - η^1 : η^2 . As displayed in Figure S22, carboxyl oxygen atoms connect the adjacent Ce(III) ions as well as the coordinated water molecules to create a 1D chain. The chains are linked to each other axially by hydrogen bonds to form a 2D layer (Figure S23).

Structural Comparison of RC_1 – RC_5 . RC_1 – RC_5 were from two chlorophenoxyacetic acids with different substitution sites, exhibiting structural commonality as well as specific structural features. The data show that all five compounds belong to the monoclinic system. Two types of coordination modes, μ_2 - η^1 : η^1 and μ_2 - η^1 : η^2 , can be found in the carboxyl groups of RC_1 – RC_5 . Both coordinated water and lattice water exist in RC_1 – RC_5 . Importantly, the flexibility of ligands contributed by free rotation of the carbon–oxygen bond and carbon–carbon bond leads to the structural multiformity of RCs (Figure 6).

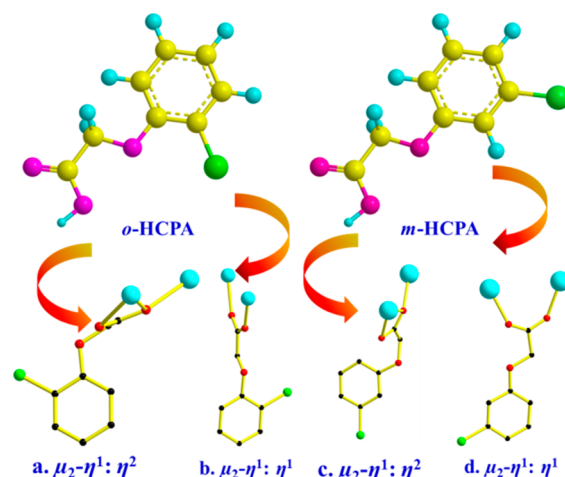


Figure 6. Two ligands and coordination modes.

Synthesis and Characterization of $SiO_2@RC$ -gal Nanocarriers. RC_1 – RC_5 were synthesized via microwaves by mixing the sodium salt of o -CPA or m -CPA and a rare-earth metal chloride. RCs were coated with a thin layer of amorphous silica by the classical reverse microemulsion method. In addition to stabilizing the spheres of the complexes, the prepared thin layer can be further decorated with β -D-galactose molecules to achieve target delivery. APTES were applied to cap holes and to introduce further modification. The SEM and TEM images of the nanocarriers are shown in Figure 7. The size distribution histogram of $SiO_2@RC_2$ -gal revealed nanoparticle sizes of 125 ± 10 nm, and the data are quite consistent with the results of SEM and TEM images (Figure 8).

The entrapment of RCs in the nanocarriers was also confirmed by infrared spectroscopy. From Figure 9, the successful immobilization of $-N_3$ and alkyne β -D-galactose on the nanocarriers can be seen from the FT-IR spectrum. The absorption band at 1087 cm^{-1} belongs to the Si–O–Si vibration of the silica; thus, it can prove the successful modification of silica on RCs. The -OH absorption bands of coordination water or lattice water molecules in the complexes are around 3400 cm^{-1} . The band at 2925 cm^{-1} can be assigned to the $-\text{CH}_2-$ groups. The curve of $SiO_2@RC-N_3$ demonstrates the characteristic asymmetric azide stretch at 2105 cm^{-1} , which fully proves the existence of the azide group.

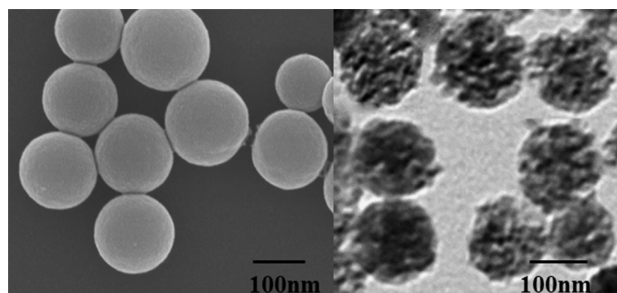


Figure 7. SEM (left) and TEM (right) images of $\text{SiO}_2@\text{RC}_2\text{-gal}$.

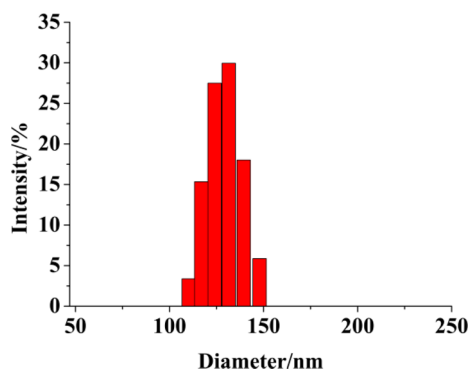


Figure 8. Size distribution of $\text{SiO}_2@\text{RCs-gal}$.

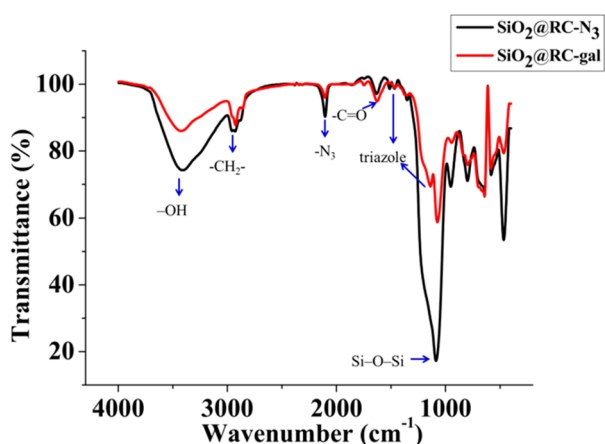


Figure 9. FT-IR spectra of $\text{SiO}_2@\text{RC-N}_3$ and $\text{SiO}_2@\text{RC-gal}$.

The $-\text{C}=\text{O}$ absorption band at 1630 cm^{-1} could be ascribed to the carboxyl groups of the ligands. Besides the significant reduction of the intensity of the alkyne peak, two sharp peaks at 1464 and 1438 cm^{-1} ascribed to the triazole fragment are observed, which indicates that through the CuAAC click reaction, $\beta\text{-D-galactose}$ has been perfectly linked to the surface of the nanoparticles.

Confocal Laser Scanning Microscopy (CLSM) Imaging. It was difficult to perform imaging because of the weak fluorescence of RC_2 . To simulate this procedure of nanoparticle distribution, we chose DOX-HCl with a strong fluorescence to replace RC_2 . The synthesis of $\text{SiO}_2@\text{DOX-gal}$ was the same as that of $\text{SiO}_2@\text{RC}_2\text{-gal}$. In Figure 10, the results show that through diffusion, free DOX-HCl crosses the cell membrane and accumulates in the HepG2 cell nuclei, thereby giving rise to cell death. DOX-HCl delivered by $\text{SiO}_2@\text{DOX-gal}$ was localized in the nuclei and cytosol of the HepG2 cells, which was ascribed to the cellular uptake behavior of

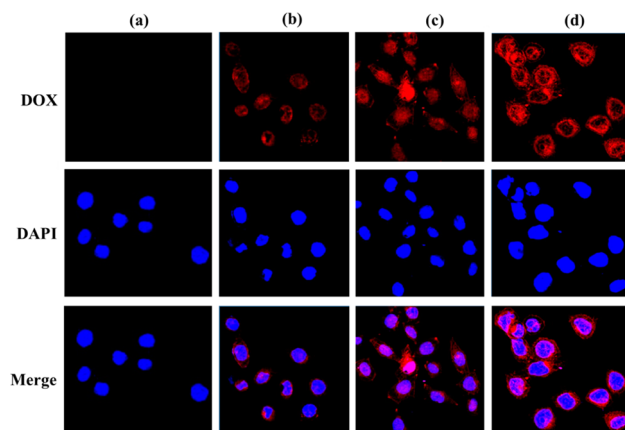


Figure 10. Confocal laser scanning microscopy images. The HepG2 cells were incubated with (a) the control, (b) DOX-HCl, (c) $\text{SiO}_2@\text{DOX-gal}$, and (d) $\text{SiO}_2@\text{RC}_2\text{-gal}$. The concentration of DOX-HCl is 10 mM . Red signal, DOX; blue signal, DAPI. The scale bar is 50 nm .

nonspecific endocytosis mechanism. Compared to that, DOX-HCl delivered by $\text{SiO}_2@\text{DOX-gal}$ was mainly localized in the cytosol. Dotted strong fluorescence was observed within the cytoplasm, which indicated that the SiO_2 spheres were trapped in the endocytic vesicles. The fluorescence images (Figure 10b–d) show that DOX-HCl (free or carried with $\text{SiO}_2\text{-gal}$) have distinctly different intracellular distributions, which should be ascribed to the distinctly different cellular uptake behavior.

In Vitro Drug Release. Via analysis of confocal laser scanning microscopy results, as Figure 10 shows, intense fluorescence was observed for $\text{SiO}_2@\text{DOX-gal}$ -treated cells in group d, while weaker fluorescence was detected for the free DOX-HCl-treated cells in group b. This result clearly shows that more DOX-HCl was taken into HepG2 cells by being loaded in the nanoparticles. This could be interpreted that the cellular uptake pathway of DOX-HCl (RC_2) and $\text{SiO}_2@\text{DOX-gal}$ ($\text{SiO}_2@\text{RC}_2\text{-gal}$) is different (passive diffusion for DOX-HCl/ RC_2 and endocytosis for $\text{SiO}_2@\text{DOX-gal}/\text{SiO}_2@\text{RC}_2\text{-gal}$). Compared to the passive diffusion of DOX-HCl/ RC_2 , the specific interaction between the galactose on the nanoparticles and the ASGP-R on the HepG2 cell surface could enhance the endocytosis efficiency of anticancer drugs. Therefore, it could be predicted that targeted nanocarriers could contribute to the enhanced cytotoxicity of anticancer drugs.

In Vitro HepG2 Cells and 293T Cell Viability Assay. The activity of $\text{RC}_1\text{--RC}_5$ (same volume of deionized water as a control) at a concentration of $10\text{ }\mu\text{g/mL}$ was studied in HepG2 cells, and the final results are shown in Figure 11. After incubation for 24 h, all five complexes ($\text{RC}_1\text{--RC}_5$) were confirmed to have good activity. In most cases, metal complexes inhibit cell growth by disturbing DNA replication. At the same time, the literature has demonstrated that chlorophenoxyacetic acid can interact with nucleic acid; therefore, we speculate that the antitumor mechanisms of the five RCs were same as those mentioned above.

Evaluating the toxicity of the vehicles in the drug delivery system is crucial. As a result of the MTT assay (Figure 12), after co-incubation with $\text{SiO}_2\text{-gal}$ for 24 h, there is no obvious cytotoxicity of $\text{SiO}_2\text{-gal}$ spheres, which was observed in the cell viabilities of HepG2 or 293T cells even up to a concentration of $300\text{ }\mu\text{g/mL}$. From this analysis, it was safe for RC delivery.

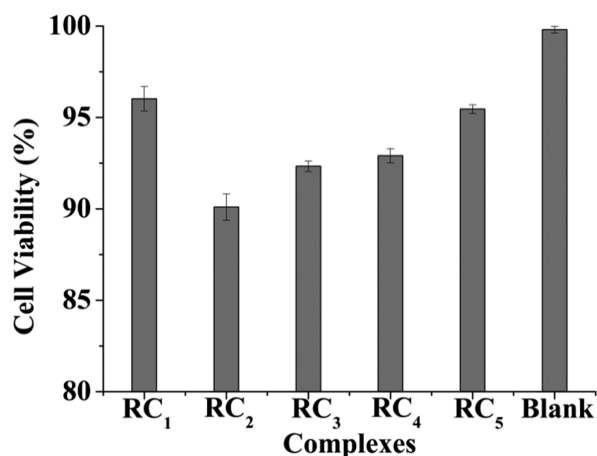


Figure 11. Cytotoxicity of five RCs and a blank control group.

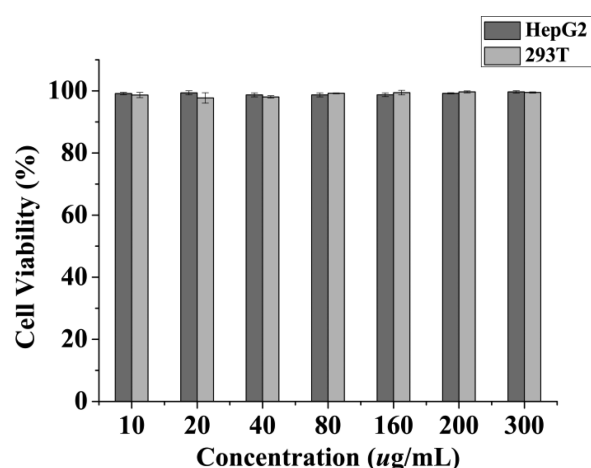


Figure 12. Cytotoxicity of SiO₂@RC₂-gal.

All five complexes (RC₁–RC₅) showed a certain anticancer effect on the HepG2 cancer cells. We take complex 2 (named RC₂) as an example described in detail. HepG2 cell survival was also estimated after incubation for 24 h with increased concentrations of the SiO₂@RC₂-gal spheres by means of the MTT assay. Strong growth inhibitory effects were observed after co-incubation. In a weakly acidic environment of the cells, the SiO₂-gal shell will gradually collapse and thus slowly release the RCs. Figure 13 shows the cell viabilities against SiO₂@RC₂-gal at RC₂ concentrations of 10, 50, 100, 150, and 200 µg/mL. It can be seen from the results, at all test concentrations, that SiO₂@RC₂-gal is more active than RC₂, because of the enhanced cellular uptake (β -D-galactose receptor-mediated endocytosis) and the EPR effect, as well as the different behavior of cellular uptake and drug release among them. It is noticed that SiO₂@RC₂-gal can effectively deliver RC₂ into HepG2 cells, leading to an improved anticancer therapeutic efficacy compared to that of free RC₂. Conjugation of β -D-galactose to the surface of the SiO₂@RC₂-N₃ can provide great potential for decreasing the side effects caused by targeted therapy.

To prove the β -D-galactose receptor-mediated property of SiO₂@RC₂-gal in cancer cells, 293T cells and HepG2 cells were treated with SiO₂@RC₂-gal. In Figure 14, SiO₂@RC₂-gal showed a high toxicity to HepG2 cells. This phenomenon can be explained in comparison with that in normal 293T cells; the

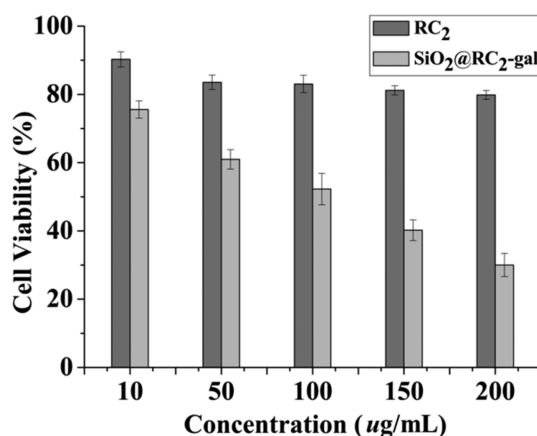


Figure 13. Cytotoxicity of RC₂ and SiO₂@RC₂-gal.

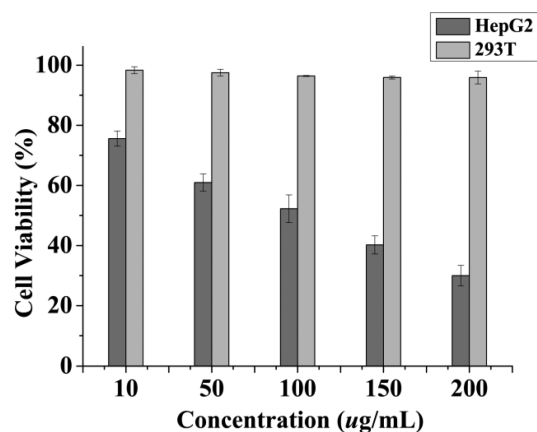


Figure 14. Cytotoxicity of SiO₂@RC₂-gal.

surfaces of human liver tumor cell line HepG2 overexpress the asialoglycoprotein receptor (ASGP-R), which specifically binds to β -D-galactose of the SiO₂@RC₂-gal nanoparticles, thus leading to stronger cytotoxicity.

CONCLUSIONS

In this work, five novel RCs with antitumor activity were prepared by a rapid microwave synthesis method. Crystal structures were characterized by single-crystal XRD and described in detail. A targeted RC delivery system that can encapsulate these complexes into the spheres was successfully developed. Via the CuAAC click reaction, the alkyne β -D-galactose was successfully grafted to the surface of the nanoparticles to achieve target delivery. Moreover, CLSM imaging results showed that receptor-mediated endocytosis leads to enhanced anticancer efficiency in HepG2 cancer cells but a lower cytotoxicity to normal 293T cells. The tumor-targeting β -D-galactose-conjugated spheres have good prospects for application in the targeted delivery of the anticancer complex and cell imaging. Further work on the design of novel RCs used for anticancer therapy with this approach is underway in our laboratory.

ASSOCIATED CONTENT

Supporting Information

The Supporting Information is available free of charge on the ACS Publications website at DOI: 10.1021/acs.inorgchem.8b01335.

Part of the synthetic routes, IR spectra, ^1H and ^{13}C NMR spectra, crystal data for $\text{RC}_1\text{--RC}_5$, crystal diagrams (Figures S17–S31), a release curve (Figure S32), and additional data (PDF)

Accession Codes

CCDC 1561412, 1561424, 1561426, and 1561432–1561433 contain the supplementary crystallographic data for this paper. These data can be obtained free of charge via www.ccdc.cam.ac.uk/data_request/cif, or by emailing data_request@ccdc.cam.ac.uk, or by contacting The Cambridge Crystallographic Data Centre, 12 Union Road, Cambridge CB2 1EZ, UK; fax: +44 1223 336033.

AUTHOR INFORMATION

Corresponding Author

*E-mail: shuaiqi@nwsuaf.edu.cn.

ORCID

Qi Shuai: 0000-0002-1910-0488

Notes

The authors declare no competing financial interest.

ACKNOWLEDGMENTS

This work was supported by the National Natural Science Foundation of China (Grants 21473136 and 21103140).

REFERENCES

- (1) Krikavova, R.; Vanco, J.; Travnicsek, Z.; Buchtik, R.; Dvorak, Z. Copper(II) quinolinonato-7-carboxamido complexes as potent antitumor agents with broad spectra and selective effects. *RSC Adv.* **2016**, *6*, 3899–3909.
- (2) Gibson, D. Platinum(IV) anticancer prodrugs – hypotheses and facts. *Dalton T.* **2016**, *45*, 12983–12991.
- (3) Zamora, A.; Perez, S. A.; Rothmund, M.; Rodriguez, V.; Schobert, R.; Janiak, C.; Ruiz, J. Exploring the Influence of the Aromaticity on the Anticancer and Antivascular Activities of Organoplatinum(II) Complexes. *Chem. - Eur. J.* **2017**, *23*, 5614–5624.
- (4) Rosenberg, B.; Van Camp, L. The successful regression of large solid sarcoma 180 tumors by platinum compounds. *Cancer Res.* **1970**, *30*, 1799–1802.
- (5) Esposito, M.; Collecchi, P.; Brera, S.; Mora, E.; Mazzucotelli, A.; Cutolo, M.; Oddone, M. Plasma and tissue levels of some lanthanide elements in malignant and non-malignant human tissues. *Sci. Total Environ.* **1986**, *50*, 55–63.
- (6) Hirano, S.; Suzuki, K. T. Exposure, metabolism, and toxicity of rare earths and related compounds. *Environ. Health Perspect.* **1996**, *104*, 85–95.
- (7) Beyer, G. J.; Franke, W. G.; Hennig, K.; Johannsen, B. A.; Khalkin, V. A.; Kretschmar, M.; Lebedev, N. A.; Munze, R.; Novgorodov, A. F.; Thieme, K. Comparative kinetic studies of simultaneously injected ^{67}Tm - and ^{67}Ga -citrate in normal and tumour bearing mice. *Int. J. Appl. Radiat. Isot.* **1978**, *29*, 673–681.
- (8) Xu, Z.; Mao, X.; Jia, L.; Xu, J.; Zhu, T.; Cai, H.; Bie, H.; Chen, R.; Ma, T. Synthesis, characterization and anticancer activities of two lanthanide (III) complexes with a nicotino-hydrazone ligand. *J. Mol. Struct.* **2015**, *1102*, 86–90.
- (9) Zhou, J.; Wang, L. F.; Wang, J. Y.; Tang, N. Synthesis, characterization, antioxidative and antitumor activities of solid quercetin rare earth (III) complexes. *J. Inorg. Biochem.* **2001**, *83*, 41–48.
- (10) Xu, D.; Ma, S.; Du, G.; He, Q.; Sun, D. Synthesis, characterization, and anticancer properties of rare earth complexes with Schiff base and o-phenanthroline. *J. Rare Earths* **2008**, *26*, 643–647.
- (11) Hussain, A.; Gadadhar, S.; Goswami, T. K.; Karande, A. A.; Chakravarty, A. R. Photo-induced DNA cleavage activity and remarkable photocytotoxicity of lanthanide (III) complexes of a polypyridyl ligand. *Dalton T.* **2012**, *41*, 885–895.
- (12) Wang, L.; Li, W. J.; Song, Y. M. Antitumor activity and DNA binding studies on rare earth metal complexes with all-trans retinoic acid and L-glutamic acid. *RSC Adv.* **2014**, *4*, 42285–42292.
- (13) Miller-Shakesby, D. M.; Burke, B. P.; Nigam, S.; Stasiuk, G. J.; Prior, T. J.; Archibald, S. J.; Redshaw, C. Synthesis, structures and cytotoxicity studies of *p*-sulfonatocalix [4] arene lanthanide complexes. *CrystEngComm* **2016**, *18*, 4977–4987.
- (14) Hussain, A.; Gadadhar, S.; Goswami, T. K.; Karande, A. A.; Chakravarty, A. R. Photoactivated DNA cleavage and anticancer activity of pyrenyl-terpyridine lanthanide complexes. *Eur. J. Med. Chem.* **2012**, *50*, 319–331.
- (15) Kumar, S.; Garg, S.; Sharma, R. P.; Venugopalan, P.; Tenti, L.; Ferretti, V.; Nivellet, L.; Tarpin, M.; Guillon, E. Four monomeric copper(II) complexes of non-steroidal anti-inflammatory drug Ibuprofen and N-donor ligands: syntheses, characterization, crystal structures and cytotoxicity studies. *New J. Chem.* **2017**, *41*, 8253–8262.
- (16) Yang, C.; Wang, W.; Liang, J.; Li, G.; Vellaisamy, K.; Wong, C.; Ma, D.; Leung, C. A rhodium (III)-based inhibitor of lysine-specific histone demethylase 1 as an epigenetic modulator in prostate cancer cells. *J. Med. Chem.* **2017**, *60*, 2597–2603.
- (17) Gill, M. R.; Thomas, J. A. Ruthenium (II) polypyridyl complexes and DNA—from structural probes to cellular imaging and therapeutics. *Chem. Soc. Rev.* **2012**, *41*, 3179–3192.
- (18) Ali, A.; Kamra, M.; Bhan, A.; Mandal, S. S.; Bhattacharya, S. New Fe (III) and Co (II) salen complexes with pendant distamycins: selective targeting of cancer cells by DNA damage and mitochondrial pathways. *Dalton T.* **2016**, *45*, 9345–9353.
- (19) Choi, S.; Yu, J. Understanding interactions between cellular matrices and metal complexes: methods to improve silver nanodot-specific staining. *Chem. - Eur. J.* **2016**, *22*, 12660–12664.
- (20) Wang, X.; Ramstrom, O.; Yan, M. Glyconanomaterials: synthesis, characterization, and ligand presentation. *Adv. Mater.* **2010**, *22*, 1946–1953.
- (21) Takara, M.; Toyoshima, M.; Seto, H.; Hoshino, Y.; Miura, Y. Polymer-modified gold nanoparticles via RAFT polymerization: a detailed study for a biosensing application. *Polym. Chem.* **2014**, *5*, 931–939.
- (22) Sharon, N. Carbohydrates as future anti-adhesion drugs for infectious diseases. *Biochim. Biophys. Acta, Gen. Subj.* **2006**, *1760*, 527–537.
- (23) Ohtsubo, K.; Marth, J. D. Glycosylation in cellular mechanisms of health and disease. *Cell* **2006**, *126*, 855–867.
- (24) Marradi, M.; Chiodo, F.; Garcia, I.; Penades, S. Glyconanoparticles as multifunctional and multimodal carbohydrate systems. *Chem. Soc. Rev.* **2013**, *42*, 4728–4745.
- (25) Shao, C.; Li, X.; Pei, Z.; Liu, D.; Wang, L.; Dong, H.; Pei, Y. Facile fabrication of glycopolymer-based iron oxide nanoparticles and their applications in the carbohydrate–lectin interaction and targeted cell imaging. *Polym. Chem.* **2016**, *7*, 1337–1344.
- (26) Yang, R.; Meng, F. H.; Ma, S. B.; Huang, F. S.; Liu, H. Y.; Zhong, Z. Y. Galactose-Decorated Cross-Linked Biodegradable Poly(ethylene glycol)-*b*-poly(ϵ -caprolactone) Block Copolymer Micelles for Enhanced Hepatoma-Targeting Delivery of Paclitaxel. *Biomacromolecules* **2011**, *12*, 3047–3055.
- (27) LEE, Y. C.; LEE, R. T. Carbohydrate-protein interactions: basis of glycobiology. *Acc. Chem. Res.* **1995**, *28*, 321–327.
- (28) Parry, A. L.; Clemson, N. A.; Ellis, J.; Bernhard, S.; Davis, B. G.; Cameron, N. R. ‘Multicopy Multivalent’ Glycopolymer-Stabilized Gold Nanoparticles as Potential Synthetic Cancer Vaccines. *J. Am. Chem. Soc.* **2013**, *135*, 9362–9365.
- (29) Yilmaz, G.; Becer, C. R. Glyconanoparticles and Their Interactions with Lectins. *Polym. Chem.* **2015**, *6*, 5503–5514.
- (30) Kohara, K.; Yamamoto, S.; Seiberg, L.; Murakami, T.; Tsujimoto, M.; Ogawa, T.; Kurata, H.; Kageyama, H.; Takano, M.

Carboxylated SiO₂-coated α -Fe nanoparticles: towards a versatile platform for biomedical applications. *Chem. Commun.* **2013**, 49, 2563–2565.

(31) Chen, D.; Li, L. L.; Tang, F. Q.; Qi, S. O. Facile and scalable synthesis of tailored silica “nanorattle” structures. *Adv. Mater.* **2009**, 21, 3804–3807.

(32) Arrachart, G.; Karatchevtseva, I.; Cassidy, D. J.; Triani, G.; Bartlett, J. R.; Chi Man, M. W. Synthesis and characterisation of carboxylate-terminated silica nanohybrid powders and thin films. *J. Mater. Chem.* **2008**, 18, 3643–3649.

(33) Gao, F. G.; Li, L. L.; Liu, T. L.; Hao, N. J.; Liu, H. Y.; Tan, L. F.; Li, H. B.; Huang, X. L.; Peng, B.; Yan, C. M.; Yang, L. Q.; Wu, X. L.; Chen, D.; Tang, F. Q. Doxorubicin loaded silica nanorattles actively seek tumors with improved anti-tumor effects. *Nanoscale* **2012**, 4, 3365–3372.

(34) Lin, C. H.; Cheng, S. H.; Liao, W. N.; Wei, P. R.; Sung, P. J.; Weng, C. F.; Lee, C. H. Mesoporous silica nanoparticles for the improved anticancer efficacy of cis-platin. *Int. J. Pharm.* **2012**, 429, 138–147.

(35) Moitra, N.; Trens, P.; Raehm, L.; Durand, J. O.; Cattoen, X.; Chi Man, M. W. Facile route to functionalized mesoporous silicananoparticles by click chemistry. *J. Mater. Chem.* **2011**, 21, 13476–13482.

(36) Brevet, D.; Gary-Bobo, M.; Raehm, L.; Richeter, S.; Hocine, O.; Amro, K.; Loock, P.B.; Couleaud, P.; Frochot, C.; Morère, A.; Maillard, P.; Garcia, M.; Durand, J.-O. Mannose-targeted mesoporous silica nanoparticles for photodynamic therapy. *Chem. Commun.* **2009**, 12, 1475–1477.

(37) Hong, C. Y.; Li, X.; Pan, C. Y. Fabrication of smart nanocontainers with a mesoporous core and a pH-responsive shell for controlled uptake and release. *J. Mater. Chem.* **2009**, 19, 5155–5160.

(38) Jian, G.; Liu, Y.; He, X.; Chen, L.; Zhang, Y. Click chemistry: a new facile and efficient strategy for the preparation of Fe₃O₄ nanoparticles covalently functionalized with IDA-Cu and their application in the depletion of abundant protein in blood samples. *Nanoscale* **2012**, 4, 6336–6342.

(39) Quinton, D.; Maringa, A.; Griveau, S.; Nyokong, T.; Bedioui, F. Surface patterning using scanning electrochemical microscopy to locally trigger a “click” chemistry reaction. *Electrochem. Commun.* **2013**, 31, 112–115.

(40) Eren, O.; Gorur, M.; Keskin, B.; Yilmaz, F. Synthesis and characterization of ferrocene end-capped poly(ϵ -caprolactone)s by a combination of ring-opening polymerization and “click” chemistry techniques. *React. Funct. Polym.* **2013**, 73, 244–253.

(41) Qiu, S. Y.; Gao, S.; Liu, Q. D.; Lin, Z. Y.; Qiu, B.; Chen, G. N. Electrochemical impedance spectroscopy sensor for ascorbic acid based on copper (I) catalyzed click chemistry. *Biosens. Bioelectron.* **2011**, 26, 4326–4330.

(42) Sai Sudhir, V.; Phani Kumar, N. Y.; Chandrasekaran, S. Click chemistry inspired synthesis of ferrocene amino acids and other derivatives. *Tetrahedron* **2010**, 66, 1327–1334.

(43) Park, C.; Lee, K.; Kim, C. Photoresponsive Cyclodextrin-Covered Nanocontainers and Their Sol-Gel Transition Induced by Molecular Recognition. *Angew. Chem.* **2009**, 121, 1301–1304.

(44) Park, C.; Kim, H.; Kim, S.; Kim, C. Enzyme Responsive Nanocontainers with Cyclodextrin Gatekeepers and Synergistic Effects in Release of Guests. *J. Am. Chem. Soc.* **2009**, 131, 16614–16615.

(45) Sheldrick, G. M. Crystal structure refinement with SHELXL. *Acta Crystallogr., Sect. C: Struct. Chem.* **2015**, 71, 3–8.

(46) Galán, L. A.; Reid, B. L.; Stagni, S.; Sobolev, A. N.; Skelton, B. W.; Cocchi, M.; Malicka, J. M.; Zysman-Colman, E.; Moore, E. G.; Ogden, M. I.; Massi, M. Visible and Near-Infrared Emission from Lanthanoid β -Triketonate Assemblies Incorporating Cesium Cations. *Inorg. Chem.* **2017**, 56, 8975–8985.

(47) Lucaccini, E.; Baldoví, J. J.; Chelazzi, L.; Barra, A. L.; Grepioni, F.; Costes, J. P.; Sorace, L. Electronic Structure and Magnetic

Anisotropy in Lanthanoid Single-Ion Magnets with C₃ Symmetry: The Ln (trenovan) Series. *Inorg. Chem.* **2017**, 56, 4728–4738.